Reaction Mechanisms of La2NiO4+δ Oxygen Electrodes Operated in Electrolysis and Fuel Cell Mode

Giuseppe Sdanghi, Lydia Yefsah, Fabrice Mauvy, Elisabeth Djurado, Thomas David, Jean-Marc. Bassat, Jérôme Laurencin

Reaction mechanisms of $La_2NiO_{4+\delta}$ oxygen electrodes operated in electrolysis and fuel cell mode

G. Sdanghi[a,b*], L. Yefsah[b,c], F. Mauvy[a], E. Djurado[c], T. David[b], J-M. Bassat[a], J. Laurencin[b]

[a]CNRS, Univ. Bordeaux, ICMCB, 87 Av. Dr. Schweitzer, 33608 Pessac, France

[b]Univ. Grenoble Alpes – CEA, LITEN, DTCH, 17 rue des Martyrs, 38054, Grenoble, France

[c]CNRS, Univ. Grenoble Alpes, LEPMI, 1130 Rue de la Piscine, 38402, Saint Martin d'Hères, France

Abstract.

The reaction mechanisms governing the electrochemical behavior of $La_2NiO_{4+\delta}$ (LNO) oxygen electrodes for Solid Oxide Cells have been investigated through a coupled experimental and modeling approach. In this frame, a set of experiments was performed on a symmetrical cell using a three-electrode setup. A micro-scale electrode model considering two reaction pathways, *i.e.* bulk and surface paths, has been developed to describe the experimental results. The microstructural parameters of the electrode were obtained by FIB-SEM tomography. The model was calibrated using the experimental polarization curves measured at different temperatures, and it was validated using electrochemical impedance diagrams recorded at open circuit potential (OCP) and under polarization for different oxygen partial pressures.

It has been evidenced that the LNO reaction mechanism depends on both the temperature and the polarization. At OCP, the reaction mechanism is controlled by the bulk path at 650 °C and by the surface path at higher temperatures. A transition from the bulk path towards the surface path was observed under cathodic polarizations. These results have been interpreted by considering the evolution of the LNO over stoichiometry with the electrode polarization. The evolution of the electrode polarization resistance with the oxygen partial pressure has been also investigated.

Keywords: Oxygen electrode reaction, nickelates, SOFC, SOEC, Modeling, EIS, polarization curves.

*Corresponding author: Telephone: +33 4 38 78 61 97, E-mail: giuseppe.sdanghi@cnrs.fr

1. Introduction

Solid Oxide Cells (SOCs) are electrochemical devices that can be used either in fuel cell (SOFCs for Solid Oxide Fuel Cells) or electrolysis modes (SOECs for Solid Oxide Electrolysis Cells). Thanks to their high operating temperature (750°C-850°C), they can reach high electrical efficiencies without using expensive electrocatalysts [1]. The SOCs are composed of a thin and dense electrolyte classically made of Yttria Stabilized Zirconia (YSZ), which is sandwiched between two porous electrodes. The hydrogen electrode is usually a porous cermet of nickel and YSZ (Ni-YSZ), while Mixed Ionic and Electronic Conductors (MIECs) are currently used for the oxygen electrodes. Indeed, MIEC electrodes lead to improve the electrochemical properties of the SOCs [2,3] if compared to other types of the electrode [3–5]. In this frame, the lanthanum doped strontium cobalt ferrite $La_{1-x}Sr_xCo_{y-1}Fe_yO_{3-\delta}$ (LSCF) is nowadays the most classical material employed as an oxygen electrode in commercial cells [6–9]. LSCF materials are oxygen deficient oxides, with a high electronic conductivity occurring by hole hopping and non-negligible ionic conduction involving oxygen vacancies. Although LSCF is well-suited for SOCs applications, this material suffers from chemical decomposition, consisting in migration and segregation of Sr'_{La} from the perovskite lattice resulting in the formation of a SrO insulating film at the LSCF surface, blocking the reactions of oxygen exchange herein [10,11]. These phenomena are known to decrease the SOC lifetime especially under electrolysis mode [11].

Considering another type of MIEC oxides, rare earth nickelates $Ln_2NiO_{4+\delta}$ (Ln = La, Pr, Nd), belong to an alternative promising family of materials with oxygen over stoichiometry [12]. The oxygen-excess crystalline structure of nickelates, which consists of alternating rock salts LnO and perovskite $LnNiO_3$ layers, can provide a very high mixed oxygen ionic and electronic conductivity (≈ 100 S cm^{-1} at 700 °C) [2,13] with fast oxygen reduction reaction kinetics [14–19]. This structure has a strong ability to accept interstitial oxygen even at high temperature, which is located in the LnO rock-salt interlayers, thus maintaining structural stability [20]. The aforementioned features allow significantly improving the cell electrochemical performance, especially at intermediate temperatures (600-700°C). Out of all nickelates electrodes, $La_2NiO_{4+\delta}$ (LNO) is the most chemically stable in a wide range of temperature and oxygen partial pressure. Indeed, LNO always keeps a K_2NiF_4-type structure, the symmetry only changing from orthorhombic to tetragonal around 150 °C under air or 400 °C at $pO_2=10^{-4}$ atm, as shown by Flura et al. [21]. Conversely, solid oxide materials rich in praseodymium were found to be chemically unstable in the temperature range 600-800 °C, since they progressively

decompose into various perovskite-derived components, such as Pr_6O_{11}, $PrNiO_{3-\delta}$, $Pr_4Ni_3O_{10+\delta}$, and NiO [22,23]. Among the different studied nickelates, $La_2NiO_{4+\delta}$ can be thus considered as the reference material.

In addition, both the electrode architecture and its microstructure play a key role in the electrochemical behavior of the MIEC-type electrodes. Therefore, several recent experimental studies have been devoted to optimize the LNO material [14,24–29]. Sayers et al. [24] have obtained a polarization resistance (R_{pol}) value equal to 1 $\Omega\,cm^2$ at 700 °C under air and at zero dc current for screen printed (SP) electrodes deposited on a dense Gadolinium-doped Ceria (GDC) electrolyte. Vibhu et al. [14] reported in the same experimental condition R_{pol} = 0.3 $\Omega\,cm^2$ for a SP electrode layered on a YSZ electrolyte. Besides, Nicollet et al. [25] have shown that preparing composite electrodes *via* the infiltration of LNO in a GDC backbone is a very promising manufacturing route to increase significantly the electrochemical performance of the SOFC cathodes. Indeed, the authors obtained R_{pol} = 0.38 $\Omega\,cm^2$ at 600 °C (under air and zero dc current) when using a YSZ electrolyte. Furthermore, R_{pol} decreased down to 0.29 $\Omega\,cm^{-2}$ at 600°C when adding a GDC interlayer between the composite electrode and the YSZ electrolyte. Such a difference arises from the formation of a thick insulating $La_2Zr_2O_7$ layer when the electrode is directly in contact with the electrolyte, downgrading the ionic transfer at the electrode/electrolyte interface. Sharma et al. [26] have measured R_{pol} = 0.42 $\Omega\,cm^2$ at 600°C (under air and at zero dc current) when using LNO electrodes deposited on GDC electrolyte by Electrostatic Spray Deposition (ESD) topped by a SP LNO current collector. When a composite interface LNO/GDC was designed between this previous double-layered LNO electrode and GDC, a decrease of R_{pol} value down to 0.16 $\Omega\,cm^2$ at 600°C was recorded [27].

The performances of the LNO oxygen electrode can thus be significantly improved by microstructural optimization. In this objective, a deep knowledge of the reaction mechanisms is necessary to identify the most adapted microstructure enhancing the electrode response. Therefore, several theoretical and experimental studies have been dedicated to investigating the electrochemical mechanisms of MIEC electrodes, especially for the LSCF material [30–34].

A general modeling framework describing the electrochemical behavior of MIEC oxygen electrodes (*i.e.* working either in fuel cell and electrolysis modes) has been already developed by our research group [32,35,36]. In the recent past, it has been applied to propose a micro-scale physically based model for both LSCF and composite LSCF-CGO electrodes. Such a model has been found to predict accurately the electrochemical response of the LSCF and LSCF-CGO porous electrodes, giving a thorough description of the reaction mechanism taking place herein.

Conversely to LSCF, the reaction mechanisms of LNO oxygen electrodes operating in both fuel cell and electrolysis modes are still not precisely understood [37,38]. Indeed, only a few experimental studies dealing with the electrochemical behavior of this electrode material under polarization are currently available in the literature [39]. Moreover, to the best of our knowledge, electrochemical models have not yet been proposed for over-stoichiometric materials such as nickelates.

The present work aims to better understand the reaction mechanisms occurring in LNO oxygen electrodes operating under both anodic and cathodic polarization through the aforementioned modeling approach adapted for the LNO material. For this purpose, experiments have been firstly performed by using a three electrodes setup. Polarization curves (η-i) have been recorded at different temperatures (650 – 750 °C) under air. EIS diagrams were also measured at the OCP and under both anodic and cathodic polarization. In addition, the impact of the oxygen partial pressures on the electrode performance has been also investigated at 700°C. The electrode microstructural properties have been extracted from 3D reconstruction obtained by Focused Ion Beam – Scanning Electron Microscopy (FIB-SEM) tomography. The polarization curves and the EIS diagrams at OCP and under cathodic and anodic polarization have been then simulated with the model. The impact of the temperature and the polarization on the reaction pathway have been investigated. The model has been also used to simulate the variation of the electrode polarization resistance with respect to the oxygen partial pressure.

2. Materials and methods

2.1 Description of the electrochemical cell

A symmetrical button cell (Figure 1) was manufactured with $La_2NiO_{4+\delta}$ electrodes deposited by Screen-Printing (SP) on each side of a circular and dense 8YSZ electrolyte (diameter: 25 mm, thickness: 260 µm, provider: Neyco). The LNO powder was first prepared *via* the citrate-nitrate route (modified Pechini method) [40], from La_2O_3 (Strem Chemical, 99,99%) and $Ni(NO_3)_2{\cdot}6H_2O$ (Acros Organics, 99%) precursors. La_2O_3 was pre-fired in the first step at 900 °C for 12 hours to remove the water content. Final annealing was performed at 1200 °C for 12 hours in the air to form the crystalline phase. A milling step by attrition was carried out to decrease the mean particle size of the powder to reach a particle size distribution ranging from 0.5 µm to 1 µm. Then, screen-printing terpineol-based slurries were prepared using LNO as well as $Ce_{0.8}Gd_{0.2}O_{2-\delta}$ (CGO) powders (provided by Solvay company in this latter case). Indeed,

a CGO barrier layer of 2 µm of thickness was previously added by screen printing between LNO and 8YSZ to limit the formation of the insulating phase $La_2Zr_2O_7$ between the electrode and the electrolyte (the sintering of the CGO layer was performed at 1300°C for 1h under air). The LNO containing slurry was used to deposit the electrodes on each side of the 8YSZ membrane. A two-step sintering process under air was then performed: (i) 400 °C for 1 h, with a heating rate of 1 °C min^{-1}, which allowed removing the organic solvent; and (ii) 1150 °C for 1 h with a heating rate of 2 °C min^{-1} to ensure the sintering on YSZ / CGO. The good adhesion between the cell layers has been checked on a cell cross-section observed by Scanning Electron Microscopy (SEM) (Figure S1a). To avoid any misalignment between the working and counter electrodes (WE and CE, respectively), special attention was paid to ensure the electrodes positioned on the electrolyte center. This feature is fundamental to avoid any perturbation and errors on the EIS measurements [41]. After manufacturing, the thickness of the LNO electrode was around 35 µm, while its diameter was ≈ 11.3 mm (thus the obtained surface area was around 1 cm^2).

2.2 Experimental setup and testing conditions

The electrochemical characterization of the symmetrical cell has been performed using a three electrodes setup, as shown in Figure 1. A platinum wire ring, used as a reference electrode (RE), was positioned on the upper surface of the electrolyte, on the periphery of the membrane (*i.e.*, the diameter of the Pt wire ring was ≈ 25 mm). To avoid as much as possible measurement artifacts due to the influence of the equipotential lines through the electrolyte on the RE, the distance between the WE and RE must be higher than three times the electrolyte thickness [42]. This requirement has been largely satisfied in the present work since the distance between the WE and RE is around 7 mm for an electrolyte thickness of 260 µm (Figure 1).

Two platinum grids with a mesh of 3600 meshes cm^{-2} and a surface equal to that of the symmetrical electrodes were used as current collectors on both the WE and CE. A ≈ 1 mm thick disk in porous gold was also inserted between the ceramic housing and the platinum grids so that each electrode surface can be considered as equipotential. A weight of 0.7 kg was also applied to the setup. This assembly aimed to ensure the electric contact between the metallic grids and the ceramic electrodes.

To optimize the electric contacts and to stabilize the electrochemical response, the cell was first heated up to 800 °C with a heating rate of 1 °C min^{-1} and then maintained at this temperature for 24 h, under air. The electrochemical measurements were carried out at 650 °C,

700 °C, and 750°C. A high inlet flow rate (total flow rate ~ 2 NL min^{-1}) was used to avoid oxygen depletion within the electrode under operation. The O_2 and N_2 flow rates were adjusted to make pO_2 varying in the range 0.15-1 atm.

The current density-voltage (*i-V*) curves measured between the electrodes and the reference (WE/CE *vs.* RE) were recorded first in SOEC mode, then in SOFC mode. Measurements were carried out from zero dc current to the highest polarization, then back to zero. The *i-V* curves were recorded in potentiostatic mode with a step of 2 mV s^{-1}. In complementarity to the polarization curves, EIS measurements were performed in galvanostatic mode, *i.e.* at open circuit potential (OCP) and under anodic/cathodic dc current densities. The frequency range was scanned from 10^6 to 10^{-2} Hz with a signal amplitude of ± 10 mA cm^{-2} using an Autolab potentiostat/impedance frequency analyzer (PGSTAT 302N), equipped with a frequency response analyzer (FRA). The amplitude of the sinusoidal perturbation for the impedance measurements was chosen to remain in the linear regime of the cell response. From the EIS data, the ohmic and polarization resistances (R_s and R_{pol}, respectively) have been obtained considering the intercepts of the impedance diagram with the real axis at high (R_s) and low frequencies ($R_{tot} = R_s+R_{pol}$). The overpotential of the WE at each current density, η, has been determined by subtracting the ohmic drop to the corresponding dc voltage applied, E_{WR}. Therefore, the overpotential was calculated as $\eta = E_{WR} - R_s \times i_{dc}$. After the measurements, the cell was heated up again to 800 °C, under air, and for 12 hours, to check that no significant degradation (evidenced *via* the EIS characterizations) was induced during the test campaign.

2.3 Microstructural Characterization by FIB-SEM Reconstruction

The microstructural parameters used in the model have been extracted from 3D reconstruction obtained by Focused Ion Beam – Scanning Electron Microscopy (FIB-SEM) tomography. The samples were first impregnated under vacuum conditions to fill the pores with an epoxy resin. This procedure allowed: (i) minimizing the undesirable damage of the specimen; (ii) avoiding the accumulation of gallium ions in the pores during the FIB milling and; (iii) improving the contrast between the porosity and the solid phases [43]. The serial sectioning and the image acquisition were carried out in a FEG-SEM NVISION 40 from Carl ZEISS® microscope. An energy selective backscatter (ESB) detector with a low acceleration voltage of 1.5 kV was used for the SEM observations. This condition allowed distinguishing the porosity and the solid phases. Then, images with a pixel size of 10 nm were acquired

sequentially with a z-axis slice pitch of 10 nm using a milling current of 1.5 nA. After the acquisition, the images in the stack were aligned using the Matlab® software. Finally, the raw 3D images were filtered and thresholded as described in previous work [44]. A volume of 14.43 × 18.72 × 10.1 μm^3 with a voxel size of 10 nm was selected. This resolution is sufficient to capture the small geometrical features of the electrode. The rendering volume for the reconstruction is shown in Figure 2 while a SEM image taken from the stack is given in the Supplementary Information (Figure S1b). As a first visual inspection, it is evidenced that the LNO microstructure appears homogeneous and quite typical of SOCs electrodes.

The microstructural properties needed for the model have been then computed thanks to a set of numerical tools already presented and thoroughly detailed in [45,46]. In this study, the specific surface area (S_p), the phase connectivity (δ), the volume fraction for the percolated phases (ε), the mean phase diameter (d_p), the 'apparent' tortuosity factor (τ), and the density of the Triple Phase Boundary lines (TPBls) (ξ_{TPBls}) have been calculated on the reconstruction. The microstructural properties for the LNO electrode are listed in Table I. As a general matter, it is worth mentioning that the LNO microstructural properties drop within typical values for the SOCs electrodes [47].

3. Model description

The electrochemical behavior of the LNO electrode under anodic and cathodic polarization has been simulated by using an in-house model, which considers an equivalent homogenous medium of an isothermal slice (1D) of porous LNO including the CGO barrier. The proposed model can simulate the LNO electrode response for both stationary and dynamic behavior. Because of the importance of the electrode microstructure on its electrochemical behavior, the mass transport phenomena and the kinetic constants of each reaction have been scaled up with the microstructural parameters computed on the 3D reconstruction.

3.1 Reaction mechanisms and kinetic rates

For the sake of clarity, the reaction mechanism is depicted in Figure 3 under anodic polarization (electrolysis mode) and is described hereafter. Regarding the oxygen electrode reaction in the LNO electrodes, two parallel pathways are considered. Indeed, the oxygen oxidation/reduction reaction can occur at the two-phase (gas/electrode) as well as at the triple-phase (gas/electrode/electrolyte) boundaries lines (TPBls) [48]. The former case (bulk path)

considers an ionic transfer at the electrolyte/electrode interface to form interstitial oxygen, $O_i^{''}$, in the electrode bulk (R1) (see Table II), with subsequent diffusion of the latter through the LNO bulk and a final oxygen excorporation (R2). On the other hand, the second scenario (surface path) considers that the charge transfer may proceed by reaction at the TPBls (R3). Both reaction pathways lead to the formation of adsorbed oxygen atoms on the LNO surface. A final associative desorption step allows releasing oxygen gas molecules O_2 into the electrode porosity (R4). It is worth mentioning that the oxygen mass transfer by solid-state diffusion, the gaseous, and the adsorbed oxygen atom diffusions have been also considered in the model.

All the reactions considered in the model and the corresponding kinetic rates are listed in Table II using the "Kröger-Vink notation". Each kinetic rate is expressed as the difference between the forward and the backward reactions. The reaction rate for the ionic transfer at the CGO/LNO interface (R1) describes the oxygen exchange from the CGO phase into the LNO electrode. Even if R1 is not an oxidation/reduction reaction, its kinetic rate can be expressed through a Butler-Volmer formalism as discussed in [49]. Indeed, R1 is affected by the electrode potential, *E(z)* corresponding to the difference in electronic potential $\varphi_{LNO}(z)$ and ionic potential $\varphi_{CGO}(z)$:

$$E(z) = \varphi_{LNO}(z) - \varphi_{CGO}(z) = -\frac{\tilde{\mu}_{e^-_{,LNO}}}{F} - \frac{\tilde{\mu}_{V^{\bullet\bullet}_{O,CGO}}}{2F} \quad (1)$$

where $\tilde{\mu}_{e^-_{,LNO}}$ and $\tilde{\mu}_{V^{\bullet\bullet}_{O,CGO}}$ denote the electrochemical potentials for the oxygen vacancies in CGO and for the electrons in LNO, respectively. In contrast to the ionic transfer, the oxygen exchange at the LNO surface (R2) is an oxidation/reduction reaction. However, as detailed in [32] for the LSCF, its reaction rate can be expressed as a pure chemical reaction since only neutral adsorbed oxygen atoms are considered on the electrode surface [49]. The charge transfer at the TPBls (R3) is a classical electrochemical reaction and its kinetic rate has been expressed according to the Butler-Volmer formalism. Finally, the associative desorption (R4) generates O_2 gaseous molecules in the pores of the electrode. As it is a pure chemical reaction, its kinetic rate depends only on the activity of the adsorbed species and the oxygen partial pressure. It can be noticed that an ideal solution for the surface species has been assumed in the model. In that condition, the activity of the adsorbed oxygen atoms is given by the product of the number of available sites on the LNO surface, Γ, and the surface coverage, $\theta_{O_{s,LNO}}$. In other words, a Langmuir hypothesis is adopted in the model so that $\theta_{s,LNO} + \theta_{O_{s,LNO}} = 1$.

All the kinetic rates have been scaled up by considering the electrode morphological properties. For instance, the oxygen excorporation reaction (R2) and the desorption one (R4) are dependent on the LNO/gas specific surface area, $S_p^{LNO/gas}$, since they both take place on the electrode surface. Conversely, the charge transfer reaction at TPBls (R3) is directly proportional to the density of active TPBls, ξ_{TPBls}. Finally, the ionic transfer reaction at the electrode/electrolyte interface (R1) depends on the CGO/LNO specific surface area, $S_p^{CGO/LNO}$. All the reactions are supposed to be thermally activated. Therefore, each kinetic constant is supposed to depend on the temperature according to Arrhenius's law.

3.2 Thermodynamic description

In the model, the forward and backward kinetic constants for each reaction are linked through the thermodynamic equilibrium constants according to the expressions listed in Table III, which represent the reaction quotients at the equilibrium state. In these equations, the electrode potential at equilibrium, E^{eq}, is equal to the chemical potential of oxygen in the gas phase taken at the reference electrode (i.e., $E^{eq} = \frac{\tilde{\mu}_{O_2,gas}^{ref}}{4F}$, as discussed in [50]). The surface coverage of the adsorbed oxygen atoms at equilibrium, $\theta_{O_{s,LNO}}^{eq}$, is considered as a model input parameter at pO_2=0.21 atm, and it is obtained by fitting the experimental polarization curves. Moreover, the oxygen coverage is assumed as independent of the temperature. This hypothesis is justified as long as the oxygen coverage remains low on the surface sites, with no restriction. Knowing $\theta_{O_{s,LNO}}^{eq}$ at pO_2=0.21 atm, the equilibrium constant $K_e^{(4)}$ can be determined, and hence, the evolution of $\theta_{O_{s,LNO}}^{eq}$ as a function of the oxygen partial pressure can be computed with Eq. 9.

To calculate the composition at equilibrium, the concentration of interstitial oxygen ${c_{O_i''}}^{eq}$ is determined as a function of the temperature using the available data of the oxygen over stoichiometry, δ^{eq}, and the volume of the lattice unit-cell, V (${c_{O_i''}}^{eq} = \delta^{eq}/V$) at pO_2 = 0.21 atm [51]. This approach allows calculating the thermodynamic equilibrium constant $K_e^{(2)}$ at the three investigated temperatures. Hence, the evolution of ${c_{O_i''}}^{eq}$ as a function of the oxygen partial pressure can be computed at each temperature by using Eq. 7.

Finally, the thermodynamic equilibrium constants $K_e^{(1)}$and $K_e^{(3)}$are calculated with Eqs. 6 and 8 by using the data at equilibrium.

3.3 Transport phenomena and conservation equations

The equations related to the fluxes, currents, mass, and charges balances, which are taken into account in the model, are given in Table IV. The ionic current in CGO and the electronic current in LNO have been computed using a classical Ohm's law. Specifically, the electronic conductivity in LNO has been assumed to be independent of the temperature, whereas a power law was considered to take into account its evolution with the pO_2, i.e., $\sigma_{e^-} = \sigma_0(p_{O_2})^k$. According to the data reported by Jeon et al. [52], the exponent k of the aforementioned power law is roughly about 1/10 within the range of pO_2 considered in the present study, i.e., 0.15 – 1 atm.

The transport of the interstitial oxygen in the LNO lattice has been modeled using a classical Fick's law through chemical diffusivity depending on the oxygen partial pressure:

$$D_{chem} \approx \gamma \cdot D_{O_i''} = -\frac{1}{2}\frac{\partial \ln(p_{O_2})}{\partial \ln(c_{O_i''})} \cdot D_{O_i''} \tag{10}$$

In Eq. 10, γ is the so-called thermodynamic factor. It can be noticed that the oxygen self-diffusion coefficient, $D_{O_i''}$, is directly related to the oxygen tracer coefficient through $D^* = f \cdot D_{O_i''}$, where f is the correlation factor. When it is assumed that oxygen diffuses *via* an interstitial mechanism, as in the specific case of LNO electrodes, f can be approximated to the unity [53]. Therefore, D_{chem} was calculated through Eq. 10 by using the available data for D^* provided by Li et al. [54]. D^* is thermally activated, and can be described by an Arrhenius's law. According to the authors, the corresponding activation energy is $E_a \approx 90$ kJ mol^{-1}.

The diffusivity of the oxygen adsorbed on the LNO surface, D_{Os}, as well as the ionic conductivity of the CGO barrier, σ_{CGO}, have been also supposed to be thermally activated. The evolution of σ_{CGO} as a function of the temperature was taken into account in the model using activation energy of E_a = 65 kJ mol^{-1}, as proposed in [55]. On the other hand, there is still a lack of information about the diffusivity of the oxygen atoms adsorbed on the LNO surface. Therefore, it has been considered as a model input parameter and obtained by fitting the experimental polarization curves.

It is important to highlight that all the effective transport parameters (*i.e.*, the effective conductivities and diffusivities) have been expressed as a function of their intrinsic values and the electrode microstructural parameters listed in Table I.

Finally, the gas transport in the electrode porosity has been computed in the frame of the Dusty Gas Model (DGM), combining the molecular and the Knudsen diffusion. The binary coefficient D_{O_2,N_2} can be expressed according to Fuller's theory as follows (Eq. 11):

$$D_{O_2,N_2} = \frac{0.00143}{P_{tot} \cdot \left(\left(V_{O_2}\right)^{1/3} + \left(V_{N_2}\right)^{1/3} \right)^2 \cdot \sqrt{\frac{2}{\frac{1}{M_{O_2}} + \frac{1}{M_{N_2}}}}} \cdot T^{1.75} \quad (11)$$

where M_i is the molar mass for the gas species and V_i the Fuller diffusion volume, which can be found in [56]. On the other hand, the Knudsen coefficient is given by:

$$D_{k,O_2} = \bar{r}_{pores} \cdot \frac{2}{3} \sqrt{\frac{8 \cdot RT}{\pi M_i}} \quad (12)$$

where $\bar{r}_{pores}$ is the mean pore radius.

The set of equations for the reaction rates (Eqs. 2-5), charge and mass balances (Eqs. 18-22) and the corresponding fluxes (Eqs. 13-17) represents a set of Partial Differential Equations (PDEs) that have been solved in the time domain by the Finite Element Method (FEM). The used boundary conditions for each calculated species are given in Table V. The methodology for the calculations of the EIS diagrams has been thoroughly described elsewhere [33].

4. Experimental results and model validation

4.1 Experimental results

The experimental electrode polarization curves $\eta = f(i)$ measured at 650 °C, 700 °C and 750 °C under air are shown in Figure 4a. As expected, the electrode overpotential significantly decreases when increasing the temperature for a given current density, meaning that the LNO performance is strongly thermally activated. Indeed, under SOEC conditions, an overpotential equal to +0.055 V/Pt/air was recorded at 650 °C and 0.1 A cm^{-2}, whereas a value of +0.02 V/Pt/air was obtained in the same condition at 750 °C. Hence, a relative decrease of about 64% was achieved. A higher improvement can be observed under cathodic polarization (SOFC

mode). The overpotential obtained at 750 °C and -0.1 A cm^{-2} is about four times lower than that obtained at 650 °C (-0.021 vs. -0.091 V/Pt/air, thus giving a decrease of around 77%).

The polarization curves present a dissymmetry with respect to the OCP at 700 °C and 650°C, in full agreement with the results reported by Tong et al. [39] for LNO electrodes. In other words, the performance of the LNO electrode is higher in anodic conditions, thus for electrolysis application. On the other hand, the polarization curve exhibits an almost linear behavior at 750 °C. This result is likely due to the narrow investigated overpotentials range, which is not sufficiently extended to detect a change in the slope. The strong dissymmetry of the polarization curve detected at 650°C is better highlighted in the $R_{pol} = f(\eta)$ plot (Figure 4b). This behavior may suggest a change either in the reaction mechanism or in the rate-determining step under these conditions, which would be triggered under cathodic polarization. On the other hand, the linearity of the polarization curve observed at 750 °C and in the range of considered overpotentials may suggest the presence of a unique dominant mechanism with the same co-limitations whatever the polarization.

To go further in the analysis, EIS diagrams have been acquired at OCP under air for the three investigated temperatures (Figure 5). The measured electrode polarization resistance was found to decrease from 0.78 Ω cm^2 at 650°C down to 0.20 Ω cm^2 at 750°C, in good agreement with the polarization curves. The obtained EIS diagrams present a kind of Gerischer-type element at 650 °C, whereas they exhibit a more depressed semi-circle at higher temperatures (700 and 750°C). The recorded change in the shape of the open circuit EIS diagrams when increasing the temperature is in full agreement with the results of Tong et al. [39]. This evolution suggests that the reaction mechanism at zero dc current is significantly affected by the temperature. Indeed, the characteristic frequency also increases when increasing the temperature (i.e., $f_c \approx 11$ Hz, 19 Hz, and 46 Hz at 650°C, 700 °C, and 750°C, respectively), as shown in the diagrams reported in Figure 5d to 5f. This behavior has been also observed with LSCF oxygen electrodes [9,35,57].

The EIS diagrams were also recorded under both anodic and cathodic polarization at intermediate temperature, *i.e.* at 700 °C (Figure 6). Although the EIS diagram recorded under "high" anodic polarization (+100 mA cm^{-2}) appears to be slightly depressed, the global shape does not completely change in the investigated range of overpotentials. The values for the characteristic frequencies under cathodic polarization were only slightly higher than those obtained under anodic polarization (i.e. $f_c \approx 23$ Hz at i_{dc} = - 100 A cm^{-2} and $f_c \approx 19$ Hz at i_{dc} = + 100 A cm^{-2}). However, these values remain quite close to each other. These observations may suggest that no changes in the reaction mechanism arise at an intermediate temperature in LNO electrodes in the range of investigated polarizations (i_{dc} = +/- 100 mA cm^{-2}). It is worth

mentioning that the aforementioned behavior observed for the LNO electrode is radically different from that observed for the LSCF electrodes [36]. In the latter case, the shape of the EIS diagrams was found to change from a well-defined Gerischer element at OCP towards a semi-circle under anodic current. Hence, this change was explained by a modification of the dominant reaction mechanism.

In addition to the experimental characterization previously described, the effect of the oxygen partial pressure on the LNO electrode response has been also investigated. Figure 7a shows the impedance diagrams in the Nyquist plots obtained at intermediate temperature (700°C) and OCP recorded in the pO_2 range of 0.15 - 1 atm and from 10^{-1} to 10^3 Hz. As expected, the electrode polarization resistance decreases when increasing the oxygen partial pressure. For instance, a value of about 0.41 Ω cm^2 was obtained at pO_2 = 0.21, whereas a lower value (0.28 Ω cm^2) was measured at pO_2 of 1 atm. Based on kinetic considerations, the relationship between the electrode polarization resistance, R_{pol}, and the oxygen partial pressure has been considered, using the following power law:

$$\frac{1}{R_{pol}} \propto {p_{O_2}}^n \tag{33}$$

When plotting R_{pol} as a function of pO_2, a power law with an exponent n close to 1/4 (≈ 0.23) was obtained at 700°C and OCP (Figure 7b). To the best of our knowledge, no values of the exponent n were reported for the LNO oxygen electrode yet. Indeed, only a few experimental studies dealing with the electrochemical behavior of this electrode material at OCP are currently available in the literature. Very few studies consist in fitting the impedance diagrams using an equivalent circuit with several contributions in series, each composed of resistance in parallel with a constant phase element (R//CPE) [37,38]. This approach is different than the one used in the present study. Therefore, the results obtained cannot be directly compared.

4.2 Calibration and validation of the electrochemical model

For the electrochemical simulations, all the microstructural parameters were obtained from the 3D reconstruction of the LNO electrode (Table I).

Concerning the transport properties for the mass and the charge transfer, the oxygen molecular diffusion, as well as the Knudsen diffusion coefficient, were calculated as a function

of the temperature by using Equations 11 and 12, respectively. The evolution of the chemical diffusivity D_{chem} as a function of the oxygen partial pressure was calculated using Eq. 10 while its temperature dependence was evaluated with the activation energy reported in [54]. The evolution of the electronic conductivity in LNO, σ_{e^-}, as a function of the oxygen partial pressure was obtained from the available data in [52]. Specifically, a pre-factor $\sigma_0 \approx 86$ S cm^{-1} and an exponent k of 0.07 were used. The evolution of the ionic conductivity in CGO with temperature was taken from [55] with an activation energy of 65 kJ mol^{-1}. Conversely, the diffusivity of the adsorbed oxygen on the LNO surface was considered as a model input parameter.

Concerning the thermodynamic calculation, the LNO oxygen over stoichiometry data, δ^{eq}, as a function of the temperature and at $pO_2 = 0.21$ atm were taken from Nakamura et al. [51]. The lattice unit cell volume, V, was taken from Flura et al. [21]. The resulting data for $c_{O_i''}{}^{eq}$ at the three investigated temperatures and $pO_2 = 0.21$ atm are provided in Table VI. On the other hand, the maximum amount of over-stoichiometric oxygen in LNO was calculated through the balance of the oxygen and interstitial sub-lattice sites as proposed in [58–60]. Hence, it was supposed that the LNO saturation in interstitial oxygen is reached when $\delta^{max} \approx 2$.

For the transient simulations, the CGO/LNO double-layer capacitance, C_{dl}, has been fixed at 50 µF cm^{-2}, as estimated by Monaco et al. [36] for LSCF electrodes. Indeed, there is still a lack of information about the C_{dl} for LNO electrodes.

Regarding the kinetic parameters, the ionic transfer reaction at the CGO/LNO interface (R1) has been considered as not limiting ($k_+ >> 0$) (see Table VI). On the other hand, the kinetic constants for the oxygen incorporation/excorporation reaction (R2), the direct oxidation/reduction reaction at the TPBls (R3), and the adsorption/desorption reaction (R4) are unknown.

As a summary, the undetermined parameters are the pre-exponential factor and the activation energy of the Arrhenius law for the three kinetic constants and the oxygen surface diffusivity along with the surface coverage of the adsorbed oxygen atoms at equilibrium, $\theta_{O_{s,LNO}}^{eq}$, at $pO_2 = 0.21$ atm. These unknown parameters were determined by fitting the simulated data on the experimental polarization curves at the three investigated temperatures. All the model input and fitted values of the different parameters are listed in Table VI.

The polarization curves computed with the input parameters listed in Table VI are compared to the experimental data in Figure 4a. As a general comment, a quite good agreement was achieved between the simulations and the experiments for each temperature. To validate the

model, EIS diagrams were computed in the same conditions as the experiments without additional fitting. The calculated and experimental EIS diagrams are compared in the Nyquist plot at OCP and under polarization in Figure 5a-c and Figure 6a-d, respectively. It can be observed that the model can reproduce quite accurately the shape of the experimental EIS diagrams whatever the temperature or the polarization.

In addition, for the impedance spectra in the Bode plots, the computed and experimental frequency distributions at 700°C are compared in Figure 5d-f at OCP and in Figure 6e-h under polarization. Concerning the measurements at OCP, it can be observed that the model can reproduce the increase of the characteristic frequency with the temperature. On the other hand, the slight increase of the characteristic frequency when shifting from anodic towards cathodic polarization is also well retrieved with the model. Both behaviors can be explained by the larger contribution of the direct oxidation/reduction at TPBls over the excorporation/incorporation reactions when increasing the temperature and when increasing the dc current in the sense of cathodic polarization. This behavior will be discussed in the next section. Nevertheless, a frequency lag is observed between the simulated and the experimental diagrams. The same behavior has been also observed for LSCF electrodes [36]. The origin of this discrepancy is still not completely understood. It might be due to the uncertainty in the determination of the microstructural parameters by the 3D reconstruction. Indeed, it has been shown that the electrode microstructure can have an important impact on the frequency response [9,61]. Moreover, the frequency lag between the simulations and the experiments could be also due to the impact of the contact resistances, which are attributed to non-optimal contact between the electrode and the current collector, on the polarization resistance. This possibility is discussed in the next section.

To go further in the validation, the model has been also used to simulate the LNO electrode response when operated under different oxygen partial pressures. With this aim, EIS diagrams have been computed at OCP and intermediate temperature (700 °C) in the range of pressures of 0.15 – 1 atm. The simulated electrode polarization resistance, R_{pol}, has been plotted as a function of pO_2 in logarithmic coordinates and compared to the experimental results (Figure 7b). It can be seen that the model predicts accurately the decrease of R_{pol} when increasing the oxygen partial pressure. This good agreement is also found for the exponent of the power-law used to fit both the experimental and the simulated data (Eq. 33), even if a slight difference between the two values has been found (0.21 vs. 0.23 for the simulated and experimental n, respectively). This slight discrepancy may be due to the model assumptions considering only atomic oxygen adsorbates on the electrode surface. Indeed, according to Fleig et al. [62], the

prediction of the electrode response as a function of pO_2 is particularly improved by taking into account charge species on the MIEC surface with a full elementary description of the reaction mechanism.

As a general comment, the polarization curves for the LNO electrode have been accurately fitted by the model for the determination of the missing parameters. Once calibrated, the model was able to predict quite accurately the EIS diagrams at different temperatures (650 – 750°C) and polarization (between – 100 mA cm^{-2} and + 100 mA cm^{-2}), without any additional fitting. Moreover, the electrochemical response of the LNO with the change of pO_2 has been also predicted in good agreement with the experimental results. Despite a systematic lag in the frequency distribution, the capacity of the model to reproduce the response of the LNO electrode allows validating the main model assumptions.

5. Discussion

5.1 Effect of polarization and temperature on the reaction mechanism

To analyze the reaction mechanisms taking place in the LNO electrodes, the relative proportion of the surface to the bulk path has been expressed through the ratio ξ between the kinetic rates of direct oxidation/reduction at TPBls and that of the oxygen excorporation/incorporation:

$$\xi = \frac{v_{R3}}{\int_{z=\ell_{CGO}}^{z=\ell_{LNO}} v_{R2}} \tag{34}$$

It is reminded that the charge transfer at TPBls takes place only at the gas/electrode/electrolyte interface, whereas the oxygen excorporation/incorporation reaction occurs all over the electrode thickness. Both the kinetic rates v_{R2} and v_{R3} are a result of the simulations. Once they are calculated, it is possible to evaluate the ratio ξ. Therefore, a value of ξ lower than the unity ($\xi < 1$) means that the bulk path dominates the reaction mechanism while a ratio higher than one ($\xi > 1$) corresponds to a mechanism controlled by the surface path.

The ratio ξ is plotted as a function of the electrode overpotential in Figure 8a. Whatever the investigated temperature, ξ was found to increase while decreasing the overpotential from anodic to cathodic polarization. This behavior can be interpreted through the dependence with

the electrode overpotential of both the kinetic rates of oxygen excorporation/incorporation reaction (integrated over the whole electrode thickness) and charge transfer at TPBls (at the CGO/LNO interface) (Figure 8b). Indeed, as shown in Figure 8b, the oxygen exchange reaction becomes bounded under cathodic polarization. This behavior is related to the evolution of the oxygen over-stoichiometry in the LNO lattice with the polarization. Indeed, the electrode material is progressively depleted in interstitial oxygen from anodic to cathodic polarization, as illustrated in Figure 8c. In these conditions, the concentration of interstitial oxygen becomes nil at the electrolyte/electrode interface under cathodic polarization, so that the bulk path is limited. This behavior is explained since the rate of oxygen incorporation, which supplies the material in oxygen, is lower than the fast ionic transfer at the electrolyte interface. On the other hand, the charge transfer at TPBls is found to remain strongly activated under cathodic polarization. Nevertheless, it can be noticed that the surface path is likely to be limited at very high cathodic polarization, because of the evolution of the oxygen atoms adsorbed on the LNO surface. Indeed, the surface coverage at the LNO surface decreases with increasing the absolute value of the cathodic polarization. This evolution is explained by the limitation of the adsorption of oxygen on the LNO surface to its incorporation. Therefore, the surface path is also expected to be bounded once $\theta_{O_{s,LNO}}^{eq}$ falls to zero. However, according to Figure 8c, this condition is not reached in the investigated range of overpotentials. As a result, the surface path is strongly promoted even at the highest overpotentials investigated in the present study.

On the other hand, the two pathways remain activated under anodic polarization (Figure 8b). Indeed, the concentration of interstitial oxygen in the LNO bulk is increased from equilibrium under this polarization. Nevertheless, it is found that the oxygen over-stoichiometry remains always much lower than the saturating estimated value $\delta_{max} = 2$ [58–60] for which the bulk path is bounded. Therefore, according to the model, the bulk path will be never limited if considering reasonable anodic polarization. On the other hand, the surface coverage is also increased with increasing the anodic polarization. Nevertheless, since the oxygen coverage is very low at equilibrium, the adsorption sites are never saturated, even at very high anodic polarization. Summarizing, the higher performances of the LNO electrode in electrolysis mode compared to the fuel cell conditions (cf. section 4.1) are explained by the limitation of the bulk path under cathodic polarizations while both paths remain activated under anodic polarization.

Figure 8a also shows the impact of the temperature on the ratio of the surface to the bulk path at the three investigated temperatures. For the OCP condition, the bulk path appears to be the dominant pathway at 650 °C, whereas the reaction mechanism is controlled by the surface

path at higher temperatures, *i.e.*, at 700 °C and 750 °C. This evolution allows claiming that the contribution of the charge transfer at the TPBls in the global reaction mechanism is enhanced when increasing the temperature. This electrode behavior at OCP can be explained by the thermal activation of the reaction kinetics. According to the fitted parameters reported in Table VI, the activation energy for the charge transfer at TPBls is found to be roughly equal to 142 kJ mol^{-1}, whereas the one for the oxygen incorporation/excorporation reaction is about 62 kJ mol^{-1}. Therefore, the kinetics for the charge transfer at TPBls is strongly thermally-activated as expected [36]. These results are also confirmed by the EIS diagrams at OCP and the three investigated temperatures (Figure 5). Indeed, a Gerischer-type element has been obtained at 650 °C, whereas a more depressed semicircle can be observed at 700 °C and 750 °C. This change in the shape of the EIS diagrams for LNO electrodes when increasing the temperature at OCP was also observed by Tong et al. [39]. According to Adler et al. [30], the presence of a Gerischer-type element in the impedance diagrams of MIEC electrodes suggests that the global reaction mechanism is dominated by the bulk path. Moreover, it has been shown for the LSCF that a change from the Gerischer-type impedance towards a depressed semi-circle must be ascribed to a transition from the bulk to the surface path [36,57]. All these statements are in full agreement with the present results obtained for the LNO material and reinforce the claim of a higher contribution of the surface path when increasing the temperature.

A transition from the bulk to surface path occurs under cathodic polarization at 650 °C ($\xi = 1$ at $\eta \approx -0.01$ V/Pt/Air) and under anodic polarization at 700 °C ($\xi = 1$ at $\eta \approx +0.04$ V/Pt/Air). Concerning the results at 750 °C, no transition is observed in the range of investigated overpotentials. Hence, the reaction mechanism is entirely controlled by the surface path under these conditions. The dissymmetry of the polarization curves with respect to the OCP observed at 650°C and 700°C (Figure 5a) is thus explained by the transition in the reaction pathway. Moreover, it is essential to remind that the almost linear behavior of the polarization curve observed at 750 °C is due to the limited range of overpotential considered in the present study, which is not sufficiently extended to detect a change in the slope. As a proof of the matter, Figure 8a shows that a change in the reaction mechanism would occur at anodic polarization higher than $\eta \approx +0.1$ V/Pt/Air.

5.2 Effect of the oxygen partial pressure on the reaction mechanism

In Figure 7b, it is shown that the model can reproduce quite accurately the response of the electrode LNO when changing the oxygen partial pressure. Indeed, a reaction order *n* of about 0.23 was obtained at 700 °C and OCP from both experimental measurements and simulations. Thus, the model developed in the present work has been used to identify the rate-determining steps in the oxygen evolution reaction for $n = 0.23$ (at OCP and 700°C). It was found that the oxygen reaction is mainly co-limited by the charge transfer reactions at both the gas/electrode interface (cf. R2, Table II) and at the Triple Boundary Phase lines (cf. R3, Table II). To a lesser extent, it has been found that the oxygen diffusion in the LNO bulk also participate to the co-limitation. These results are in full agreement with other works, for which the charge transfer is the rate-determining step when $n \approx 0.25$ [63].

The effect of the oxygen partial pressure on the reaction mechanism in such electrode material has been also investigated at OCP and 700 °C. The range of investigated pO_2 is 0.15 – 1 atm. Figure 9a shows that the bulk path is promoted when increasing the oxygen partial pressure. Indeed, the ratio of the surface to bulk path globally decreases when pO_2 is increased. For instance, the ratio ξ close to the OCP is about 2 at $pO_2 = 0.15$ atm, compared to 0.8 at $pO_2 = 1$ atm.

Figure 9a evidences that the surface path remains the predominant reaction mechanism at OCP for pO_2 lower than 0.6 atm, while the bulk path controls the reaction mechanism at higher oxygen partial pressures. To interpret this result, the kinetic rates of charge transfer at TPBls and oxygen exchange at the LNO surface (integrated along the electrode thickness) have been calculated close to the OCP and plotted as a function of the oxygen partial pressure in Figure 9b. It can be noticed that the kinetic rate of the oxygen exchange reaction increases with increasing the oxygen partial pressure. This behavior can be explained by the increase of the LNO over stoichiometry, $\delta_{LNO,}$ when increasing the oxygen partial pressure, as it has been observed by Nakamura et al. [64]. Indeed, the high concentration of interstitial oxygen in the LNO lattice at high pO_2 favors the bulk path in the reaction mechanism. On the other hand, the kinetic rate for the charge transfer at the TPBls at OCP is not affected by the change of pO_2. As a result, it can be noticed that the sum of the two contributions globally increases with pO_2, which explains the decrease of the electrode polarization resistance as shown in Figure 7a.

5.3 Effect of the contact resistance on the electrode response

The non-optimal contact between the electrode and the current collector is an important factor that can significantly affect the cell performances [65]. Indeed, it is well known that a low density of contact points at the interface between the electrode and the current collector can induce high ohmic contact resistances [66]. Besides, it also affects the current distribution in the electrode [67], thus inducing a significant increase in the electrode polarization resistance [67,68]. Moreover, this effect can be exacerbated by a low electronic conductivity of the electrode material [67]. It is worth noting that the frequency distribution in the impedance diagram should not be strongly impacted by the inhomogeneous distribution of current in the electrode. Indeed, the inhomogeneous current distribution will decrease the 'effective' surface area in the electrodes where the reactions occur [69] while the overall reaction mechanism must remain identical. In other words, a non-optimal current collection will increase both the ohmic and electrode polarization resistances while the frequency response should be not changed significantly.

In the present work, the contact resistances were evaluated by removing the ohmic losses due to the electrolyte from the experimental series resistances measured on the impedance diagrams. For example, a contact resistance of 1.72 Ω.cm² was found at 700°C. This high value is explained on one hand by a very rough electrode surface limiting the density of contacts with the grid, and on the other hand, by the relative low electric conductivity of LNO compared to other electrode materials (*e.g.* LSCF, LSM) [13]. Therefore, it is reasonable to consider that the electrode polarization resistance obtained in the present work may be significantly over-estimated by the contact resistances. Thereby, the model developed in the present work has been used to minimize the influence of the contact resistance on the electrode behavior. With this aim, the model has been calibrated by fitting the experimental frequency distributions instead of the polarization curves. This approach allows identifying the electrode polarization resistances without any influence of the contact resistances. Thus, it is assumed that the electrode is governed by the same reaction mechanisms as previously described in section 5.1. The same trends of the surface-to-bulk ratio as a function of the polarization and the temperature have been retained.

By following this approach, the frequency lag shown in the previous section tends to disappear, allowing obtaining lower R_{pol} than those recorded experimentally (Figure 10 and Figure S2). According to the results reported in Figure 10, a correction factor ≈ 0.12 should be used to correct the R_{pol} recorded experimentally, confirming that the contribution of the contact

resistances to the obtained experimental measurements is effectively quite large. By fitting the experimental frequency distribution, new values of the missing model parameters (*i.e.*, i) the pre-exponential factor and ii) the activation energy of the Arrhenius law for the three kinetic constants, and iii) the oxygen surface diffusivity along with the surface coverage of the adsorbed oxygen atoms at equilibrium, $\theta_{O_{s,LNO}}^{eq}$, at pO_2 = 0.21 atm) were obtained (Table SI, Supplementary Information). The obtained values of the kinetic parameters are higher than those obtained through the fitting of the experimental polarization curves listed in Table VI (while the oxygen surface diffusivity remains identical). Indeed, a significant enhancement of the electrode performance is obtained, as shown in the polarization curves reported in Figure S3. Thus, these results could be representative of the ideal case in which the electrode behavior is not affected by any contact resistances. In other words, the kinetic constants obtained by following this approach could be considered as the intrinsic properties of the LNO material according to the reaction mechanisms considered in the present work and described in section 3. Moreover, the effect of the oxygen partial pressure on the electrode performance is also unchanged (Figure S4).

To validate the aforementioned model calibration method based on the fitting of the frequency distribution, the global chemical constant of the oxygen exchange, k_{chem}, has been calculated using the expression from the Adler model as presented in [70] and by using the polarization resistance, R_{pol} taken from the corrected impedance diagrams:

$$k_{chem} = \left(\frac{RT}{4F^2 c_{O_i''}^{eq}}\right)^2 \cdot \frac{1}{\frac{\varepsilon_{LNO}}{\tau_{LNO}} D_{chem} \cdot S_p^{LNO/gas} \cdot {R_{pol}}^2} \quad (35)$$

Using the values reported in Table I and VI for the microstructural and input parameters, respectively, and the R_{pol} obtained by fitting the frequency distribution, k_{chem} was found to be around $1.06 \cdot 10^{-5}$, $2.73 \cdot 10^{-5}$ and $6.57 \cdot 10^{-5}$ m s^{-1} at 650, 700 and 750°C, respectively. These values are in full agreement with the data of k_{chem} measured through electrical conductivity relaxation and reported in the literature [54,71]. For the sake of comparison, it is worth mentioning that the values of k_{chem} evaluated using the polarization resistances recorded experimentally are two order of magnitude lower than those of k_{chem} reported in the literature. Therefore, this discussion suggests that the frequency lag between the simulations and the experiments reported in section 4 is related to the impact of the current collection on the polarization resistance. Nevertheless, the reaction mechanism for the LNO material remains unchanged.

6. Conclusion

In this study, a coupled experimental and modeling approach has been used to investigate the reaction mechanisms of the $La_2NiO_{4+\delta}$ (LNO) oxygen electrodes.

A set of experiments has been performed by using a three-electrode setup. Polarization curves (η-i) have been recorded in the temperature range of 650-750 °C and under air. Impedance diagrams have been also recorded in the temperature range of 650-750°C, at OCP and under air. A decrease of the electrode polarization resistance from about 0.78 Ω cm^2 at 650°C down to 0.20 Ω cm^2 at 750°C was obtained. The shape of the EIS diagram changed from a Gerischer-like element at 650 °C and OCP towards a depressed semicircle at higher temperatures. The effect of the oxygen partial pressure on the LNO electrode response in the range of 0.15 - 1 atm has been also investigated.

To analyse the experimental results, a physically-based electrode model has been developed. It considers two parallel pathways, *i.e.*: (i) the oxygen incorporation/excorporation at the gas/electrode interface for the bulk path and; (ii) the direct charge transfer at the TPBls for the surface path. A 3D electrode reconstruction obtained by FIB-SEM tomography allowed determining the microstructural properties required for the simulations. With a reduced number of unknown parameters, the model has been found to reproduce the dissymmetry of the electrode polarization curves. Furthermore, without any additional fitting, the model can reproduce correctly the shape of the experimental EIS diagram at OCP and under polarization whatever the temperature. The evolution of the electrode polarization resistance with the oxygen partial pressure is also well described by the model. Nevertheless, a frequency lag was systematically obtained for the impedance diagrams. This discrepancy has been attributed to the impact of the current collection on the polarization resistance.

Once validated, the model has been used to analyze the LNO reaction mechanisms. The contribution of the charge transfer at the TPBls (surface path) over the excorporation/incorporation reaction (bulk path) was found to increase with the cathodic dc current. This evolution has been explained by the limitation of the bulk path caused by the interstitial oxygen depletion in LNO arising under cathodic current. Regarding the anodic polarization, the two pathways remain activated explaining the higher performances obtained in this condition. Moreover, the bulk path controls the reaction mechanism at OCP and 650 °C, whereas the contribution of the surface path increases while increasing the operating temperature (700 and 750 °C). A transition from the bulk to surface path occurs under cathodic polarization at 650 °C $\eta \approx -0.01$ V/Pt/Air) and under anodic polarization at 700 °C ($\eta \approx +0.04$

V/Pt/Air), in full agreement with the dissymmetry of the polarization curves recorded experimentally. Finally, the dependence of the LNO electrode response with pO_2 has been explained since the bulk path is promoted when increasing the oxygen partial pressures.

7. Acknowledgments

This study was supported by the French National Research Agency (ANR) project "ECOREVE", reference ANR-18-CE05-0036, and by the GENVIA company. The authors thank the company SRT Microcéramique for the screen-printing of the CGO barrier onto the YSZ electrolyte.

References

1. N. Minh, J. Mizusaki, and S. C. Singhal, *ECS Trans.*, **78**, 63 (2017).

2. E. Boehm, J.-M. Bassat, M. C. Steil, P. Dordor, F. Mauvy, and J.-C. Grenier, *Solid State Sci.*, **5**, 973–981 (2003).

3. I. Riess, *Solid State Ion.*, **157**, 1–17 (2003).

4. A. R. West, *J. Mater. Chem.*, **1**, 157–162 (1991).

5. A. Barbucci, P. Carpanese, G. Cerisola, and M. Viviani, *Solid State Ion.*, **176**, 1753–1758 (2005).

6. A. Ahuja, M. Gautam, A. Sinha, J. Sharma, P. K. Patro, and A. Venkatasubramanian, *Bull. Mater. Sci.*, **43**, 129 (2020).

7. A. Donazzi, G. Cordaro, A. Baricci, Z.-B. Ding, and M. Maestri, *Electrochimica Acta*, **335**, 135620 (2020).

8. H. J. Hwang, J.-W. Moon, S. Lee, and E. A. Lee, *J. Power Sources*, **145**, 243–248 (2005).

9. J. Nielsen, T. Jacobsen, and M. Wandel, *Electrochimica Acta*, **56**, 7963–7974 (2011).

10. G. Ch. Kostogloudis, G. Tsiniarakis, and Ch. Ftikos, *Solid State Ion.*, **135**, 529–535 (2000).

11. J. Laurencin, M. Hubert, D. F. Sanchez, S. Pylypko, M. Morales, A. Morata, B. Morel, D. Montinaro, F. Lefebvre-Joud, and E. Siebert, *Electrochimica Acta*, **241**, 459–476 (2017).

12. V. Vibhu, A. Rougier, C. Nicollet, A. Flura, J.-C. Grenier, and J.-M. Bassat, *Solid State Ion.*, **278**, 32–37 (2015).

13. E. Boehm, J.-M. Bassat, P. Dordor, F. Mauvy, J.-C. Grenier, and Ph. Stevens, *Solid State Ion.*, **176**, 2717–2725 (2005).

14. V. Vibhu, A. Rougier, J.-C. Grenier, and J.-M. Bassat, *ECS Trans.*, **57**, 2093 (2013).

15. Y. Lee and H. Kim, *Ceram. Int.*, **41**, 5984–5991 (2015).

16. S. J. Skinner and J. A. Kilner, *Solid State Ion.*, **135**, 709–712 (2000).

17. A. D. Rougier, A. Flura, C. Nicollet, V. Vibhu, S. Fourcade, E. Lebraud, J.-M. Bassat, and J.-C. Grenier, *ECS Trans.*, **68**, 817 (2015).

18. A. Montenegro-Hernández, J. Vega-Castillo, L. Mogni, and A. Caneiro, *Int. J. Hydrog. Energy*, **36**, 15704–15714 (2011).

19. K. Zhao, Y.-P. Wang, M. Chen, Q. Xu, B.-H. Kim, and D.-P. Huang, *Int. J. Hydrog. Energy*, **39**, 7120–7130 (2014).

20. V. V. Vashook, S. P. Tolochko, I. I. Yushkevich, L. V. Makhnach, I. F. Kononyuk, H. Altenburg, J. Hauck, and H. Ullmann, *Solid State Ion.*, **110**, 245–253 (1998).

21. A. Flura, S. Dru, C. Nicollet, V. Vibhu, S. Fourcade, E. Lebraud, A. Rougier, J.-M. Bassat, and J.-C. Grenier, *J. Solid State Chem.*, **228**, 189–198 (2015).

22. V. Vibhu, A. Flura, A. Rougier, C. Nicollet, S. Fourcade, T. Hungria, J.-C. Grenier, and J.-M. Bassat, *J. Energy Chem.*, **46**, 62–70 (2020).

23. N. I. Khamidy, J. Laurencin, D. Ferreira Sanchez, F. Monaco, F. Charlot, and E. Djurado, *J. Power Sources*, **450**, 227724 (2020).

24. R. Sayers, M. Rieu, P. Lenormand, F. Ansart, J. A. Kilner, and S. J. Skinner, *Solid State Ion.*, **192**, 531–534 (2011).

25. C. Nicollet, A. Flura, V. Vibhu, A. Rougier, J. M. Bassat, and J. C. Grenier, *J. Power Sources*, **294**, 473–482 (2015).

26. R. K. Sharma, M. Burriel, L. Dessemond, V. Martin, J.-M. Bassat, and E. Djurado, *J. Power Sources*, **316**, 17–28 (2016).

27. R. K. Sharma, M. Burriel, L. Dessemond, J. M. Bassat, and E. Djurado, *J. Mater. Chem. A*, **4**, 12451–12462 (2016).

28. N. Hildenbrand, P. Nammensma, D. H. A. Blank, H. J. M. Bouwmeester, and B. A. Boukamp, *J. Power Sources*, **238**, 442–453 (2013).

29. A. Egger, N. Schrödl, C. Gspan, and W. Sitte, *Solid State Ion.*, **299**, 18–25 (2017).

30. S. B. Adler, J. A. Lane, and B. C. H. Steele, *J. Electrochem. Soc.*, **143**, 3554 (1996).

31. M. Prestat, J.-F. Koenig, and L. J. Gauckler, *J. Electroceramics*, **18**, 87–101 (2007).

32. J. Laurencin, M. Hubert, K. Couturier, T. L. Bihan, P. Cloetens, F. Lefebvre-Joud, and E. Siebert, *Electrochimica Acta*, **174**, 1299–1316 (2015).

33. M. Hubert, J. Laurencin, P. Cloetens, J. C. da Silva, F. Lefebvre-Joud, P. Bleuet, A. Nakajo, and E. Siebert, *Solid State Ion.*, **294**, 90–107 (2016).

34. L. Ma, P. Priya, and N. R. Aluru, *J. Electrochem. Soc.*, **165**, F1232 (2018).

35. E. Effori, H. Moussaoui, F. Monaco, R. K. Sharma, J. Debayle, Y. Gavet, G. Delette, G. S. Larbi, E. Siebert, J. Vulliet, L. Dessemond, and J. Laurencin, *Fuel Cells*, **19**, 429–444 (2019).

36. F. Monaco, V. Tezyk, E. Siebert, S. Pylypko, B. Morel, J. Vulliet, T. Le Bihan, F. Lefebvre-Joud, and J. Laurencin, *Solid State Ion.*, **319**, 234–246 (2018).

37. J. S. A. Carneiro, R. A. Brocca, M. L. R. S. Lucena, and E. Nikolla, *Appl. Catal. B Environ.*, **200**, 106–113 (2017).

38. M. J. Escudero, A. Aguadero, J. A. Alonso, and L. Daza, *J. Electroanal. Chem.*, **611**, 107–116 (2007).

39. X. Tong, F. Zhou, S. Yang, S. Zhong, M. Wei, and Y. Liu, *Ceram. Int.*, **43**, 10927–10933 (2017).

40. Ph. Courty, H. Ajot, Ch. Marcilly, and B. Delmon, *Powder Technol.*, **7**, 21–38 (1973).

41. S. B. Adler, *Solid State Ion.*, **135**, 603–612 (2000).

42. S. B. Adler, B. T. Henderson, M. A. Wilson, D. M. Taylor, and R. E. Richards, *Solid State Ion.*, **134**, 35–42 (2000).

43. N. Vivet, S. Chupin, E. Estrade, T. Piquero, P. L. Pommier, D. Rochais, and E. Bruneton, *J. Power Sources*, **196**, 7541–7549 (2011).

44. J. Villanova, J. Laurencin, P. Cloetens, P. Bleuet, G. Delette, H. Suhonen, and F. Usseglio-Viretta, *J. Power Sources*, **243**, 841–849 (2013).

45. F. Usseglio-Viretta, J. Laurencin, G. Delette, J. Villanova, P. Cloetens, and D. Leguillon, *J. Power Sources*, **256**, 394–403 (2014).

46. H. Moussaoui, J. Laurencin, Y. Gavet, G. Delette, M. Hubert, P. Cloetens, T. Le Bihan, and J. Debayle, *Comput. Mater. Sci.*, **143**, 262–276 (2018).

47. J. Jochen, *Microstructural Characterisation, Modelling and Simulation of Solid Oxide Fuel Cell Cathodes*, p. 246, KIT Scientific Publishing, (2017).

48. G. W. Coffey, L. R. Pederson, and P. C. Rieke, *J. Electrochem. Soc.*, **150**, A1139 (2003).

49. A. M. Svensson, S. Sunde, and K. Nisşancioğlu, *J. Electrochem. Soc.*, **144**, 2719 (1997).

50. F. Monaco, E. Effori, M. Hubert, E. Siebert, G. Geneste, B. Morel, E. Djurado, D. Montinaro, and J. Laurencin, *Electrochimica Acta*, **389**, 138765 (2021).

51. T. Nakamura, K. Yashiro, K. Sato, and J. Mizusaki, *Solid State Ion.*, **180**, 368–376 (2009).

52. S.-Y. Jeon, M.-B. Choi, J.-H. Hwang, E. D. Wachsman, and S.-J. Song, *J. Electrochem. Soc.*, **158**, B476 (2011).

53. P. Kofstad, *Nonstoichiometry, diffusion, and electrical conductivity in binary metal oxides.*, Wiley Interscience., p. 81, New York, USA, (1972).

54. Z. Li and R. Haugsrud, *Solid State Ion.*, **206**, 67–71 (2012).

55. R. Tanaka, W. S. Oliveira, A. Brandão, J. C. C. Abrantes, and J. R. Frade, *Electrochimica Acta*, **85**, 116–121 (2012).

56. B. Todd and J. B. Young, *J. Power Sources*, **110**, 186–200 (2002).

57. E. Effori, J. Laurencin, E. D. R. Silva, M. Hubert, T. David, M. Petitjean, G. Geneste, L. Dessemond, and E. Siebert, *J. Electrochem. Soc.*, **168**, 044520 (2021).

58. M. Schroeder and M.-A. Dragan, *J. Mater. Sci.*, **42**, 1972–1983 (2007).

59. H.-S. Kim and H.-I. Yoo, *Solid State Ion.*, **232**, 129–137 (2013).

60. T. Nakamura, R. Oike, Y. Ling, Y. Tamenori, and K. Amezawa, *Phys. Chem. Chem. Phys.*, **18**, 1564–1569 (2016).

61. Özden Çelikbilek, E. Siebert, D. Jauffrès, C. L. Martin, and E. Djurado, *Electrochimica Acta*, **246**, 1248–1258 (2017).

62. J. Fleig, R. Merkle, and J. Maier, *Phys. Chem. Chem. Phys.*, **9**, 2713–2723 (2007).

63. Y. Takeda, R. Kanno, M. Noda, Y. Tomida, and O. Yamamoto, *J. Electrochem. Soc.*, **134**, 2656 (1987).

64. T. Nakamura, Y. Takeyama, S. Watanabe, K. Yashiro, K. Sato, T. Hashida, and J. Mizusaki, *ECS Trans.*, **25**, 2573 (2009).

65. N. Q. Minh, *J. Korean Ceram. Soc.*, **47**, 1–7 (2010).

66. T. Dey, D. Singdeo, M. Bose, R. N. Basu, and P. C. Ghosh, *J. Power Sources*, **233**, 290–298 (2013).

67. D. Kennouche, Q. Fang, L. Blum, and D. Stolten, *J. Electrochem. Soc.*, **165**, F677 (2018).

68. S. P. Jiang, J. G. Love, and L. Apateanu, *Solid State Ion.*, **160**, 15–26 (2003).

69. J. Sar, L. Dessemond, and E. Djurado, *Int. J. Hydrog. Energy*, **41**, 17037–17043 (2016).

70. S. B. Adler, *Chem. Rev.*, **104**, 4791–4844 (2004).

71. A. Egger and W. Sitte, *Solid State Ion.*, **258**, 30–37 (2014).

List of Symbols

Roman Symbols:

C_{dl}	Surface double layer capacitance	(F m^{-2})
$c_{O_i''}$	Concentration of interstitial oxygen in LNO	(mol m^{-3})
$c_{O_i''}{}^{eq}$	Concentration of interstitial oxygen in LNO at equilibrium	(mol m^{-3})
$c_{O_i''}{}^{max,eq}$	Maximum concentration of interstitial oxygen in LNO	(mol m^{-3})
D_{chem}	Bulk oxygen chemical diffusion coefficient in LNO	(m^2 s^{-1})
D_O^{eff}	Oxygen adsorbate diffusion coefficient in LNO	(m^2 s^{-1})
D_{k,O_2}	Knudsen diffusion coefficient	(m^2 s^{-1})
D_{O_2,N_2}	Molecular diffusion coefficient	(m^2 s^{-1})
e^-	Electrons in LNO	(–)
E	Local electrode potential	(V)
F	Faraday's constant	(C mol^{-1})
$\vec{i}_{io/e'}$	Ionic current density in CGO/Electronic current density in LNO	(A m^{-2})
K_e^i	Thermodynamic equilibrium constant for the i-th reaction	(–)
k_+	Forward reaction kinetic constants for R1	(mol m^{-2} s^{-1})
$k_{ox}^{LNO/gas}$	Forward reaction kinetic constants for R2	(s^{-1})
k_{ox}^{TPB}	Forward reaction kinetic constants for R3	(m s^{-1})
k_{des}	Forward reaction kinetic constants for R4	(s^{-1})
ℓ	Electrode thickness	(µm)
ℓ_{CGO}	Electrolyte thickness	(µm)
M_i	Molar mass for the i-th species	(g mol^{-1})
n	Reaction order	(–)
$\vec{N}_i$	Molar flux of the i-th species	(mol·m^{-2}·s^{-1})
$O_i''(LNO)$	Interstitial oxygen in the LNO lattice	(–)

$O_O^X(CGO)$	Oxygen atom in the CGO lattice	(–)
$O_{s_{LNO}}$	Oxygen ad-atom on the LNO surface	(–)
$O_{2,gas}$	Gaseous oxygen molecule	(–)
p_{O_2}	Oxygen partial pressure	(atm)
P_t	Total pressure	(atm)
$\bar{r}_{pores}$	Mean pore radius	(m)
R	Universal gas constant	(J mol^{-1} K^{-1})
R_{pol}	Polarization resistance	Ω cm^2
$S_p^{CGO/LNO}$	Specific surface area between CGO and LNO	(–)
$S_p^{LNO/gas}$	Specific surface area between LNO and gas phase	(m^{-1})
T	Absolute temperature	(K)
V_i	Fuller's volume for the i-th species	(–)
$V_i^X(LNO)$	Interstitial vacancy in the LNO lattice	(–)
$V_O^{\bullet\bullet}(CGO)$	Oxygen vacancy in the CGO lattice	(–)
$y_{(i)}$	Molar fraction of species i-th species	(–)

Greek Symbols:

$\alpha_{Ri}^{ox/red}$	Charge transfer coefficient for oxidation or reduction for the reaction Ri	(–)
Γ	Surface density of available sites on LNO	(mol m^{-2})
ε_X	Phase volume fraction for the phase X	(–)
η	Overpotential	(V)
$\theta_{O_{s_{LNO}}}$	Coverage of oxygen atoms on LNO surface	(–)
$\theta_{s_{LSCF}}$	Free sites on the LNO surface	(–)
$\theta_{O_{s_{LNO}}}^{eq}$	Coverage rate of oxygen atoms on LNO at equilibrium	(–)
$\theta_{s_{LSCF}}^{eq}$	Free site on LNO at equilibrium	(–)
$v_{(i)}$	Kinetic rate of chemical/electrochemical reaction (i) in the electrode(*) or at the electrolyte interface(**)	(*) (mol m^{-3} s^{-1}) or (**) (mol m^{-2} s^{-1})
$\tilde{\mu}_i$	Electrochemical potential	(J mol^{-1})

ξ_{TPBls}	Density of triple phase boundary lengths	(m^{-1})
σ_{e^-}	Electronic conductivity of LNO	(S m^{-1})
$\sigma_{io,\ CGO}$	Ionic conductivity of CGO	(S m^{-1})
σ_i^{eff}	Effective conductivity for the i-th species	(S m^{-1})
φ_i	Potential	(V)
τ_X	Tortuosity factor for the phase X	(–)

List of Abbreviations

CE	Counter Electrode
CGO	Ceria doped Gadolinium Oxide
EIS	Electrochemical Impedance Spectroscopy
FIB-SEM	Focused Ion Beam-Scanning Electron Microscopy
LNO	Lanthanum Nickelate
MIEC	Mixed Ionic and Electronic Conductor
OCP	Open Circuit Potential
RE	Reference Electrode
SOC	Solid Oxide Cells
SOFC	Solid Oxide Fuel Cell
SOEC	Solid Oxide Electrolysis Cell
TPBls	Triple Phase Boundary lines
WE	Working Electrode
YSZ	Yttria Stabilized Zirconia

Figures

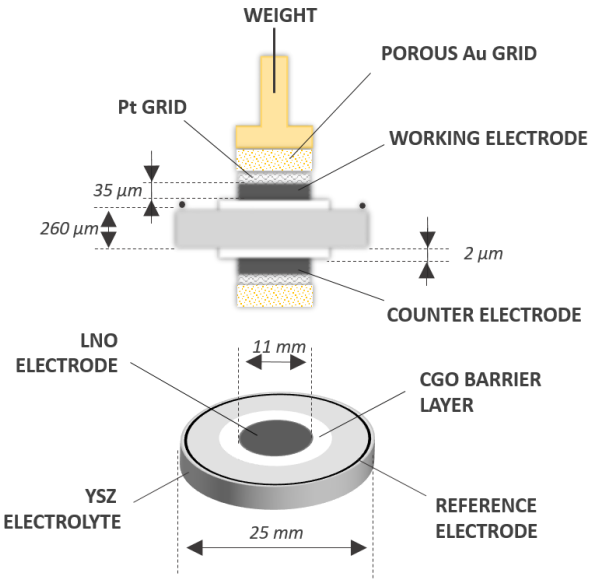

Figure 1 –Three electrode setup with a symmetrical cell configuration

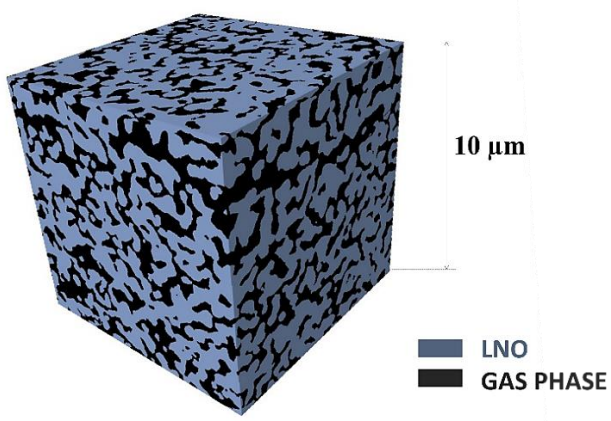

Figure 2 - 3D rendering volume for a cube of 10x10x10 µm^3 extracted from the whole LNO reconstruction

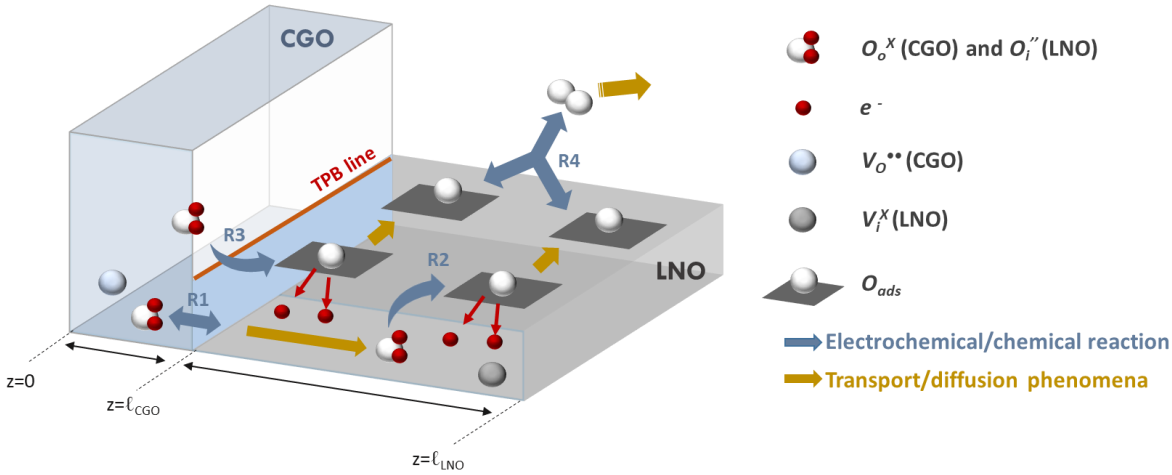

Figure 3 - Schematic description of the reaction pathway considered in the model (in electrolysis mode)

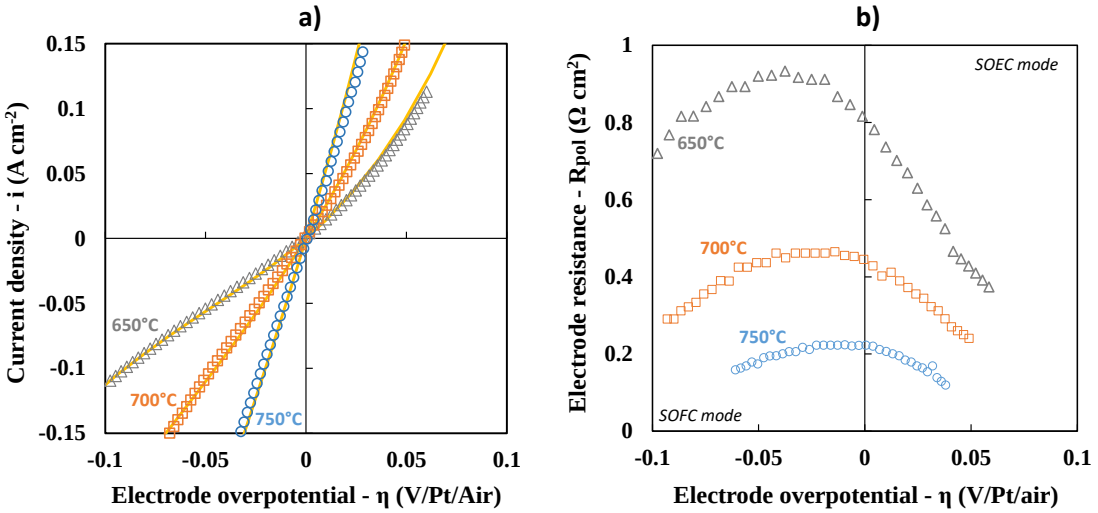

Figure 4 – a) Experimental (marks) and simulated (solid lines) polarization curves obtained at 650, 700, and 750 °C under air for LNO electrodes. b) Experimental LNO electrode polarization resistance plotted a function of the electrode overpotential for the three investigated temperatures

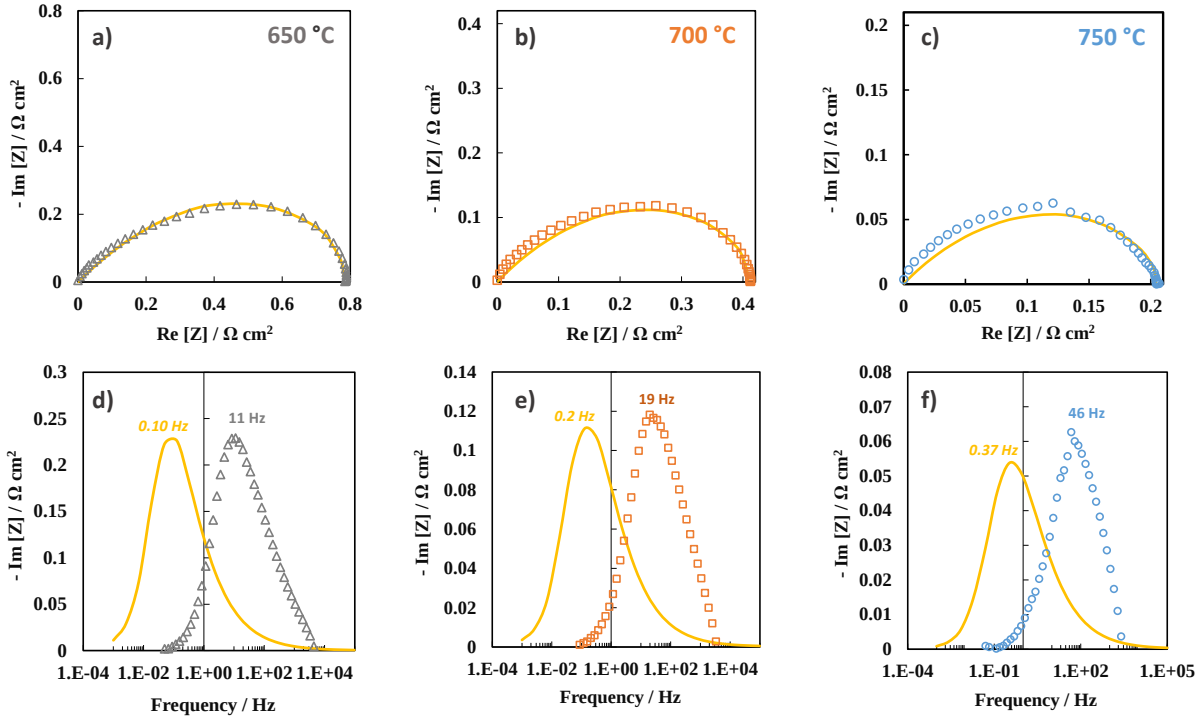

Figure 5 – Experimental (marks) and simulated (solid lines) EIS diagrams for the LNO electrodes at OCP under air. Nyquist plots for: (a) 650 °C, (b) 700 °C and (c) 750 °C. Bode plot for: (d) 650 °C, (e) 700 °C and (f) 750 °C

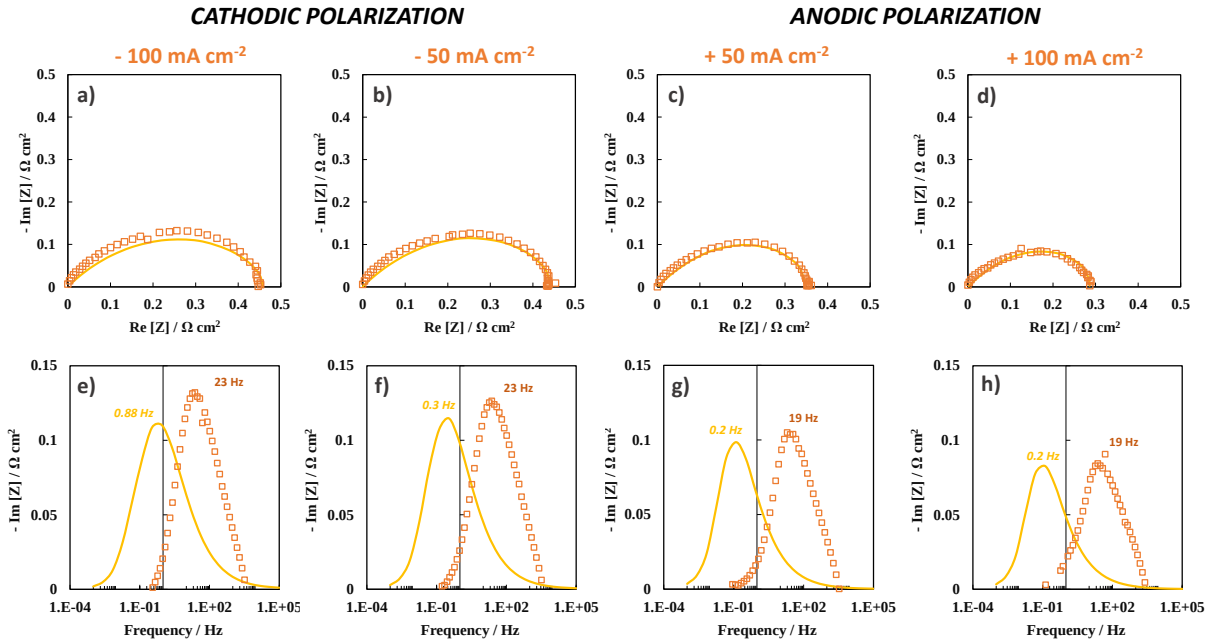

Figure 6 - Experimental (marks) and simulated (solid lines) EIS diagrams at 700 °C under air for i_{dc} = – 100 mA cm^{-2}, – 50 mA cm^{-2}, + 50 mA cm^{-2} and + 100 mA cm^{-2}. (a-d) Nyquist plots and (e-h) Bode plots

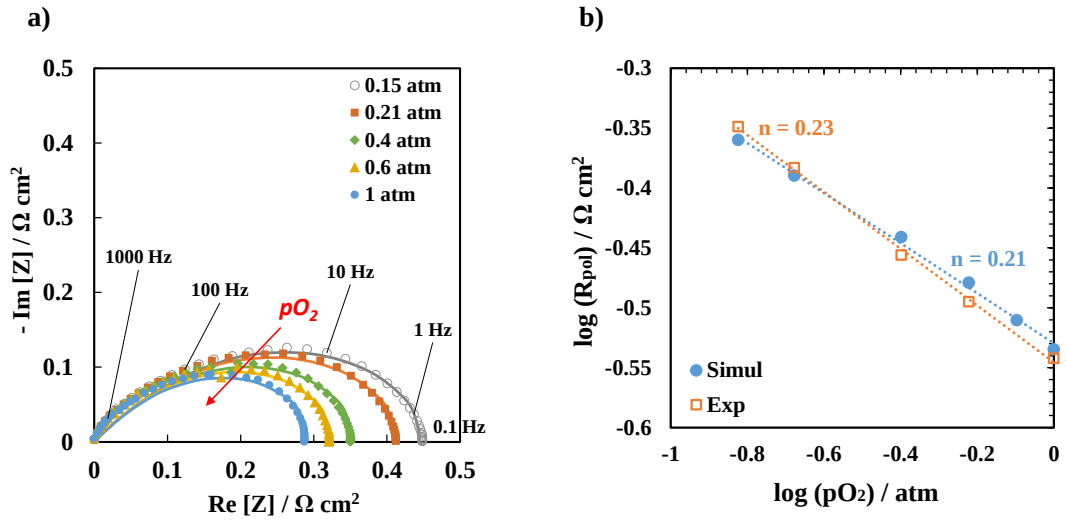

Figure 7 – a) Impedance diagrams (Nyquist plots) recorded for the LNO electrode at 700°C for the investigated range of oxygen partial pressure (marks = experimental; solid lines = simulation). b) Experimental and simulated polarization resistance plotted as a function of the oxygen partial pressure in logarithmic coordinates (at 700°C).

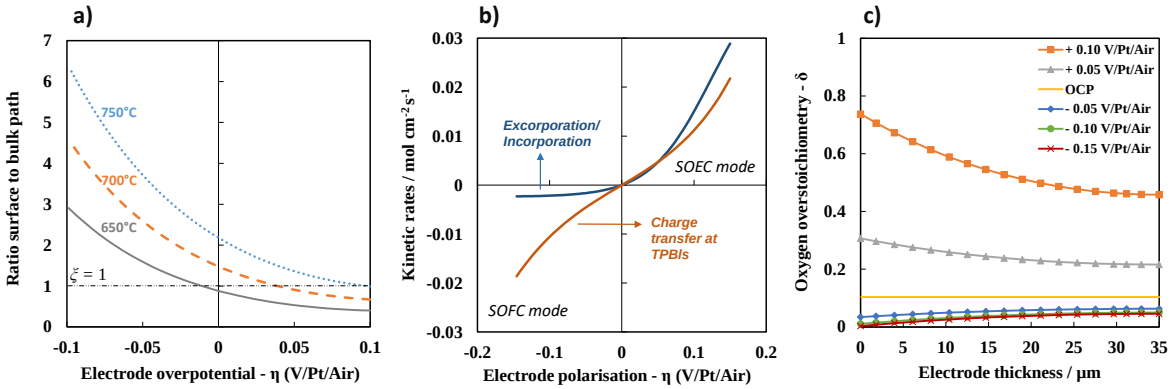

Figure 8 - a) Ratio of the surface to the bulk path under air for the LNO electrode at 650°C,700 °C and 750 °C plotted as a function of the electrode overpotential. b) Kinetics rates for the oxygen excorporation/incorporation reaction and the oxidation/reduction reaction at the TPBls as a function of the electrode overpotential at 700 °C b) Oxygen over stoichiometry in the electrode thickness at different polarization, under air and 700 °C.

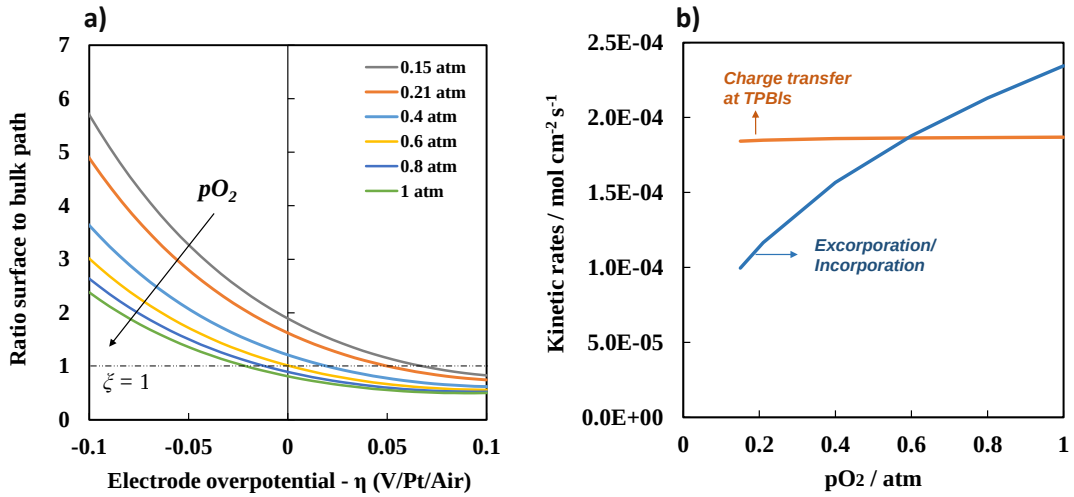

Figure 9 – a) Ratio of the surface to bulk path as a function of the electrode overpotential at OCP and 700 °C for different oxygen partial pressures. b) Kinetic rates of the oxygen excorporation/incorporation reaction and the charge transfer at TPBls as a function of pO_2 computed close to the OCP ($i_{dc} \approx 0.002$ A cm^{-2})

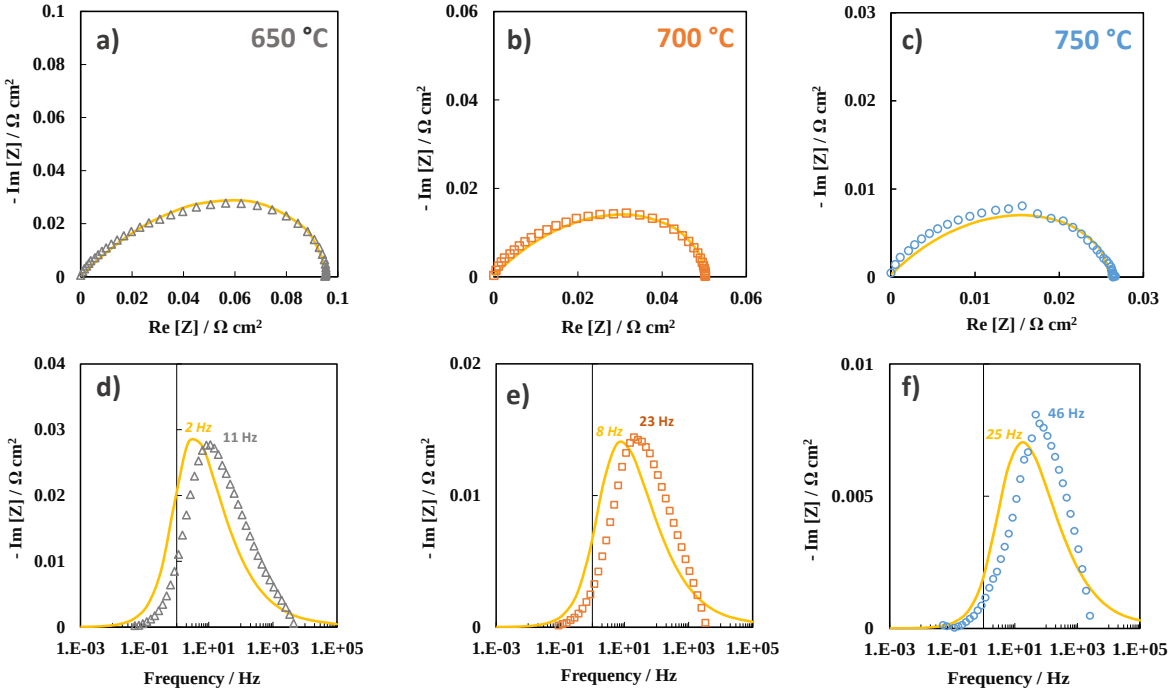

Figure 10 - EIS diagrams for the LNO electrodes at OCP under air obtained by fitting the frequency distribution. Nyquist plots for: (a) 650 °C, (b) 700 °C and (c) 750 °C. Bode plot for: (d) 650 °C, (e) 700 °C and (f) 750 °C.

Tables

Table I – Microstructural parameters of the LNO electrode reconstructed via FIB-SEM

LNO electrode										
Properties	Gas phase					MIEC (LNO)				
	S_p (μm^{-1})	δ_{gas} (%)	ε (%)	d_p (*) (μm)	τ_{gas} (-)	S_p (μm^{-1})	δ_{LNO} (%)	ε (%)	d_p (*) (μm)	τ_{LNO} (-)
FIB-SEM reconstructions	3.83	99.98	38.47	0.308	1.94	3.83	99.99	61.52	-	1.97
ξ_{TPBls} (μm^{-1})	2.51									

(*) mean phase diameter taken from the Phase Size Distribution

Table II. Reactions and expressions of the kinetics rates

Reactions		Kinetic rates	
R1	$O_O^X(CGO) + V_i^X(LNO) \underset{k_-}{\overset{k_+}{\leftrightarrow}} V_O^{\bullet\bullet}(CGO) + O_i''(LNO)$	$v_{(1)} = S_p^{CGO/LNO}\left\{k_+ exp\left(\frac{2\alpha_{(1)}^{ox} FE}{RT}\right)\left(1 - \frac{c_{O_i''}}{c_{O_i''}^{max}}\right) - k_- exp\left(\frac{-2\alpha_{(1)}^{red} FE}{RT}\right)\left(\frac{c_{O_i''}}{c_{O_i''}^{max}}\right)\right\}$	(2)
R2	$O_i''(LNO) + s_{,LNO} \underset{k_{red}^{LNO/gas}}{\overset{k_{ox}^{LNO/gas}}{\leftrightarrow}} V_i^X(LNO) + 2e^- + O_{s,LNO}$	$v_{(2)} = S_p^{LNO/gas}\left\{k_{ox}^{LNO/gas}\Gamma(1 - \theta_{O_{s,LNO}}{}^{eq})\frac{c_{O_i''}}{c_{O_i''}^{max}} - k_{red}^{LNO/gas}\Gamma\theta_{O_{s,LNO}}{}^{eq}\left(1 - \frac{c_{O_i''}}{c_{O_i''}^{max}}\right)\right\}$	(3)
R3	$O_O^X(CGO) + s_{LNO} \underset{k_{red}^{TPB}}{\overset{k_{ox}^{TPB}}{\leftrightarrow}} V_O^{\bullet\bullet}(CGO) + 2e^- + O_{s,LNO}$	$v_{(3)} = \xi_{TPBs}\left\{k_{ox}^{TPB} exp\left(\frac{2\alpha_{(3)}^{ox} FE}{RT}\right)\Gamma\left(1 - \theta_{O_{s,LNO}}{}^{eq}\right) - k_{red}^{TPB} exp\left(\frac{-2\alpha_{(3)}^{red} FE}{RT}\right)\Gamma\theta_{O_{s,LNO}}{}^{eq}\right\}$	(4)
R4	$O_{s,LNO} \underset{k_{ads}}{\overset{k_{des}}{\leftrightarrow}} \frac{1}{2}O_{2,gas} + s_{LNO}$	$v_{(4)} = S_p^{LNO/gas}\left\{k_{des}\Gamma\theta_{O_{s,LNO}}{}^{eq} - k_{ads}P_{O_2}^{1/2}\Gamma(1 - \theta_{O_{s,LNO}}{}^{eq})\right\}$	(5)

Table III – Equations for the thermodynamic equilibrium constants

Thermodynamic equilibrium constants		
R1	$K_e^{(1)} = \frac{k_+}{k_-} = \frac{c_{O_i''}{}^{eq}}{\left(c_{O_i''}{}^{max,eq} - c_{O_i''}{}^{eq}\right)} exp\left(\frac{-2FE^{eq}}{RT}\right)$	(6)
R2	$K_e^{(2)} = \frac{k_{ox}^{LNO/gas}}{k_{red}^{LNO/gas}} = \frac{\theta_{O_{s,LNO}}{}^{eq}}{1 - \theta_{O_{s,LNO}}{}^{eq}} \frac{\left(c_{O_i''}{}^{max,eq} - c_{O_i''}{}^{eq}\right)}{c_{O_i''}{}^{eq}}$	(7)
R3	$K_e^{(3)} = \frac{k_{ox}^{TPB}}{k_{red}^{TPB}} = \frac{\theta_{O_{s,LNO}}{}^{eq}}{1 - \theta_{O_{s,LNO}}{}^{eq}} exp\left(\frac{-2FE^{eq}}{RT}\right)$	(8)
R4	$K_e^{(4)} = \frac{k_{des}}{k_{ads}} = \frac{1 - \theta_{O_{s,LNO}}{}^{eq}}{\theta_{O_{s,LNO}}{}^{eq}} \left(P_{O_2}{}^{eq}\right)^{1/2}$	(9)

Table IV – Equations of charge and mass conservations associated with the current and fluxes taken into account in the physically-based model

Electrode			
Transport phenomena		**Conservation equations**	
$\vec{N}_{O_i''} = -\frac{\varepsilon_{LNO}}{\tau_{LNO}} D_{chem} \times \vec{\nabla} c_{O_i''}$	(13)	$\vec{\nabla} \cdot \vec{N}_{O_i''} = -\nu_{(2)} - \varepsilon_{LNO} \frac{\partial c_{O_i''}(z,t)}{\partial t}$	(18)
$\vec{N}_{O_{s_{LNO}}} = -S_p^{LNO/gas} \cdot D_{O_{s_{LNO}}} \cdot \Gamma \cdot \vec{\nabla} \theta_{O_{s_{LNO}}}$	(14)	$\vec{\nabla} \cdot \vec{N}_{O_{s_{LNO}}} = \left(\nu_{(2)} - \nu_{(4)}\right) - S_p{}^{LNO/gas} \Gamma \frac{\partial \theta_{O_{s_{LNO}}}(z,t)}{\partial t}$	(19)
$\vec{\nabla} y_{O_2} = -\frac{RT}{P_t}\left(\frac{\vec{N}_{O_2}}{\frac{\varepsilon_{pores}}{\tau_{pores}} D_{k,O_2}} + \frac{\vec{N}_{O_2} y_{N_2}}{\frac{\varepsilon_{pores}}{\tau_{pores}} D_{O_2,N_2}}\right)$	(15)	$\vec{\nabla} \cdot \vec{N}_{O_2} = \frac{1}{2}\nu_{(4)} - \frac{\varepsilon_{pores}}{RT} P_t \frac{\partial y_{O_2}(z,t)}{\partial t}$	(20)
$\vec{\imath}_{e^-} = -\frac{\varepsilon_{LNO}}{\tau_{LNO}} \sigma_{e^-} \times \vec{\nabla} \varphi_{LNO}$	(16)	$\vec{\nabla} \cdot \vec{N}_{O_2} = \frac{1}{2}\nu_{(4)} - \frac{\varepsilon_{pores}}{RT} P_t \frac{\partial y_{O_2}(z,t)}{\partial t}$	(21)
Electrolyte			
$\vec{\imath}_{io} = -\sigma_{io,CGO} \times \vec{\nabla} \varphi_{CGO}$	(17)	$\vec{\nabla} \cdot \vec{\imath}_{io} = 0$	(22)

Table V – Boundary Conditions for the simulations

Species	**Boundary Conditions**				
	$z = 0$	$z = \ell_{CGO}$		$z = \ell_{LNO}$	
O_i''	n.a.*	$N_{O_i''} = \nu_{(1)}$	(23)	$N_{O_i''\|z=L} = 0$	(28)
$O_{s_{LNO}}$	n.a.	$N_{O_{s_{LNO}},local} = \nu_{(3)}$	(24)	$N_{O_{s_{LNO}}\|z=L} = 0$	(29)
O_2	n.a.	$N_{O_2,local} = 0$	(25)	$C_{O_2\|z=L} = \frac{P_{O_2}}{RT}$	(30)
Electronic current in LNO, e^-	n.a.	$i_{e^-,local} = -2F\nu_{(3)} + S_p{}^{CGO/LNO} C_{dl} \frac{\partial E}{\partial t}$	(26)	$\varphi_{e^-\|z=L} = 0$	(31)
Ionic current in CGO, i_0	imposed	$i_{io,local} = +2F\left(\nu_{(1)} + \nu_{(3)}\right) - S_p{}^{CGO/LNO} C_{dl} \frac{\partial E}{\partial t}$	(27)	n.a.	(32)

*n.a. = Not applicable

Table VI – Input parameters used to fit the experimental data (pO_2 =0.21 atm)

INPUT PARAMETERS				
Parameter		**650 °C**	**700 °C**	**750 °C**
$c_{O_i''}^{eq}$	/ mol m^{-3}	450.64	427.78	405.98
$c_{O_i''}^{max,eq}$	/ mol m^{-3}	8118.52	8127.44	8134.54
σ_{el}	/ S m^{-1}	7706.85	7706.85	7706.85
σ_{CGO}	/ S m^{-1}	1.95	2.87	4.05
Γ	/ mol m^{-2}	$1\cdot10^{-5}$	$1\cdot10^{-5}$	$1\cdot10^{-5}$
C_{dl}	/ F m^{-2}	0.5	0.5	0.5
D_{chem}	/ m^2 s^{-1}	$2.04\cdot10^{-10}$	$3.7\cdot10^{-10}$	$6.37\cdot10^{-10}$

FITTED PARAMETERS					
Parameter		**650 °C**	**700 °C**	**750 °C**	**E_a [kJ mol^{-1}]**
$\theta_{O_{s_{LNO}}}^{eq}$	/ -	$4.6\cdot10^{-5}$	$4.6\cdot10^{-5}$	$4.6\cdot10^{-5}$	-
D_{Os}	/ m^2 s^{-1}	$4\cdot10^{-6}$	$6\cdot10^{-6}$	$9\cdot10^{-6}$	63
k_+	/ mol m^{-2} s^{-1}	NOT LIMITING	NOT LIMITING	NOT LIMITING	-
$k_{ox}^{LNO/gas}$	/ m^3 mol^{-1} s^{-1}	34	43	75	62
k_{ox}^{TPB}	/ m s^{-1}	$6\cdot10^{-5}$	$1.5\cdot10^{-4}$	$3.7\cdot10^{-4}$	142
k_{ads}	/ atm$^{-0.5}$ s^{-1}	$8\cdot10^{4}$	$2\cdot10^{5}$	$4\cdot10^{5}$	126